Korean J. Chem. Eng., **29**(11), 1531-1540 (2012)
DOI: 10.1007/s11814-012-0030-3

Computational fluid dynamics modeling of hydrogen production in an autothermal reactor: Effect of different thermal conditions

Sayed Reza Shabanian*, Masoud Rahimi*,†, Amin Amiri, Shahram Sharifnia***, and Ammar Abdulaziz Alsairafi******

*CFD Research Center, Chemical Engineering Department, Razi University, Kermanshah, Iran
**Department of Chemical Engineering, Kermanshah University of Technology, Kermanshah, Iran
***Catalyst Research Center, Chemical Engineering Department, Razi University, Kermanshah, Iran
****Faculty of Mechanical Engineering, College of Engineering and Petroleum, Kuwait University, Kuwait
(*Received 6 December 2011 • accepted 7 March 2012*)

Abstract−A numerical model was developed and validated to simulate and improve the reforming efficiency of methane to syngas ($CO+H_2$) in an autothermal reactor. This work was undertaken in a 0.8 cm diameter and 30 cm length quartz tubular reactor. The exhaust gas from combustion at the bottom of reactor was passed over a $Ru/\gamma\text{-}Al_2O_3$ catalyst bed. The Eddy Dissipation Concept (EDC) model for turbulence-chemistry interaction in combination with a modified standard k-ε model for turbulence and a reaction mechanism with 23 species and 39 elementary reactions were considered in the combustion model. The pre-exponential factors and activation energy values for the catalyst (Ru) were obtained by using the experimental results. The percentage of difference between the predicted and measured mole fractions of the major species in the exhaust gas from combustion and catalyst bed zones was less than 5.02% and 7.73%, respectively. In addition, the results showed that the reforming efficiency, based on hydrogen yield, was increased with increase in catalyst bed's thermal conductivity. Moreover, an enhancement of 4.34% in the reforming efficiency was obtained with increase in the catalyst bed wall heat flux from 0.5 to 2.0 kW/m^2.

Key words: CFD, Combustion, Hydrogen Production, Reforming Efficiency, Syngas

INTRODUCTION

Syngas (H_2+CO) as a main feedstock or intermediate product has been used for production of variety of materials in many chemical processes such as GTL, methanol production, etc [1,2]. Nowadays, methane reforming process is a well-known technology for the production of syngas. The major reforming processes are steam reforming (SR) [3], partial oxidation (POX) [4,5], and autothermal reforming (ATR) [2,6]. Steam reforming of methane as a conventional process for syngas production is highly endothermic and generates a syngas with high hydrogen concentration (over 70% on dry basis). Regarding difficult startup and slow response of reactor in this process, this technology is unattractive for low-volume and low-pressure hydrogen production purposes [7,8].

On the other hand, partial oxidation (POX) is an exothermic process with an easy start up as well as high carbon monoxide concentration in product stream. This process makes hot spots in the catalyst bed and emits pollutants. In autothermal reforming, both processes of partial oxidation and steam reforming are combined in a single reactor. There are two types of autothermal (ATR) reactors including ATR with catalytic partial oxidation and ATR with noncatalytic partial oxidation.

Considerable experimental and numerical studies have been undertaken in the field of catalytic methane reforming process. In the experimental part, Rabe et al. [9] investigated syngas production using low temperature catalytic partial oxidation (LTCPO) process over noble metal catalysts. They found that platinum catalysts were less active than rhodium and ruthenium catalysts and would result in lower hydrogen yield. Dantas et al. [10] studied the effect of different promoters on $Ni/CeZrO_2$ catalyst for autothermal reforming and partial oxidation of methane. In another study, Dias and Assaf [11] found that the effect of noble metals was significant on hydrogen production. Park et al. [12] investigated autothermal reforming of CH_4 for Ni-La-Zr catalysts. Their results showed that catalysts containing 3.2 wt% La_2O_3 had the highest CH_4 conversion and H_2 yield. Lee et al. [13] examined the noble metal-doped hydrotalcite-type catalyst performance in propane autothermal reforming in terms of conversion and H_2 yield in a continuous fixed-bed reactor. In another study, the kinetic rate of methane total combustion in the presence of $Pt/\delta\text{-}AL_2O_3$ catalyst for initial temperature range of 663-723 K was presented by Ma et al. [14].

On the other hand, many investigations have been carried out to model the reforming processes [15-20]. Although the concept of hydrogen production has been extensively investigated, the computational fluid dynamics (CFD) modeling of autothermal reforming has received less attention [21]. In addition, there is a lack of scientific studies about autothermal reforming process with noncatalytic POX. In this type of ATR, the preheated feed streams (H_2O+CH_4 and H_2O+O_2) are mixed in a burner located in vicinity of the place in which combustion reactions occur [22]. Then, the outlet gas of this section is passed over a catalyst to cause steam reforming reactions.

As examples of these types of modeling, Yu [23] proposed a simu-

†To whom correspondence should be addressed.
E-mail: masoudrahimi@yahoo.com

lation method for secondary reformer in industrial ammonia plant using a one-dimensional heterogeneous catalytic reaction model. Autothermal reforming of methane in the presence of Ni/Mg-Al_2O_4 catalyst was kinetically modeled by Zahedinezhad et al. [24]. In their model, reformer was divided into two sections: combustion and catalytic steam reforming sections. In the combustion section, temperature and composition were determined using 108 simultaneous elementary reactions and kinetic equations proposed by Karim et al. [25]. The authors employed the kinetic model suggested by Xu and Froment [26] in their catalytic bed section. In another study, Amirshaghaghi et al. [27] undertook a numerical study on methane combustion process in an industrial autothermal reactor. They used a two-step reaction mechanism for gas combustion with CO as the intermediate species.

In the present work, a CFD model was developed to model a second type of autothermal reformer. In modeling of catalytic bed section, the temperature dependence of the rate law parameters was taken from equations suggested by Xu and Froment [26]. The pre-exponential factors and the activation energy values for Ni catalyst were used as initial values and, ultimately, values for Ru catalyst were obtained by fitting the established model and experimental data. In addition, this study introduces the effects of catalyst bed thermal conductivity and wall heat flux on reforming efficiency.

EXPERIMENTAL WORK

1. Catalyst Preparation

In the present work, the selected catalyst was a 5% Ru supported on γ-Al_2O_3. The ruthenium catalyst was prepared by impregnation techniques using aqueous ruthenium nitrate solution. After impregnation and drying, the samples were calcined in air at 550 °C for 3 hours.

2. Experimental Apparatus

A schematic view of experimental setup is shown in Fig. 1. This setup was established to study the influences of steam-to-carbon ratio (S/C), oxygen-to-carbon ratio (O_2/C) and feed temperature on the system performance. The experimental setup consists of two flow measuring and control systems, two humidifier units, two preheater units, a quartz reactor (I.D=0.8 cm, H=30 cm), and a gas chromatograph system. The input feed to the reactor was a mixture of methane, oxygen and water. The preheated feed streams were mixed in a burner. The outlet gas of combustion was passed over the catalyst bed. To prevent heat loss from the system, the reactor was embedded in a ceramic insulating material. Moreover, for providing an adequate steam to the feed, a stainless steel evaporator was used. A PID controller, a thermocouple and an electrical heater were employed to keep the evaporator's temperature at the desired value. All experiments were carried out under atmospheric pressure.

The reactor had two main sections, including combustion and a 5 cm catalytic fixed bed. The reactor was loaded with 412 mg catalyst mixed with 852 mg silicon carbide (SiC, 60-120 mesh) as inert solid. A thermowell (stainless steel, outer diameter: 1.5 mm) equipped with a movable thermocouple was placed in the center of the catalyst bed to monitor the temperature profile along the reactor. The distance between the thermocouple well and reactor wall was 3.25 mm. The final outlet stream was analyzed using a gas chromatograph equipped with a thermal conductivity detector and two packed columns of MS and Propack-Q for detecting the CO, CO_2 and CH_4 concentration. The estimated experimental error in the reformer was ±30 °C for the temperature and ±0.8% (by volume) for the species. The error can be attributed to the incorrect calibrations, procedural variability and instrumental deficiencies.

NUMERICAL WORK

1. Computational Domain, Governing Equation and Solution Strategy

Three-dimensional numerical modeling was conducted using the commercial CFD code FLUENT 6.2.16 for its robustness and precision. In the model, the studied domain, which consists of burner,

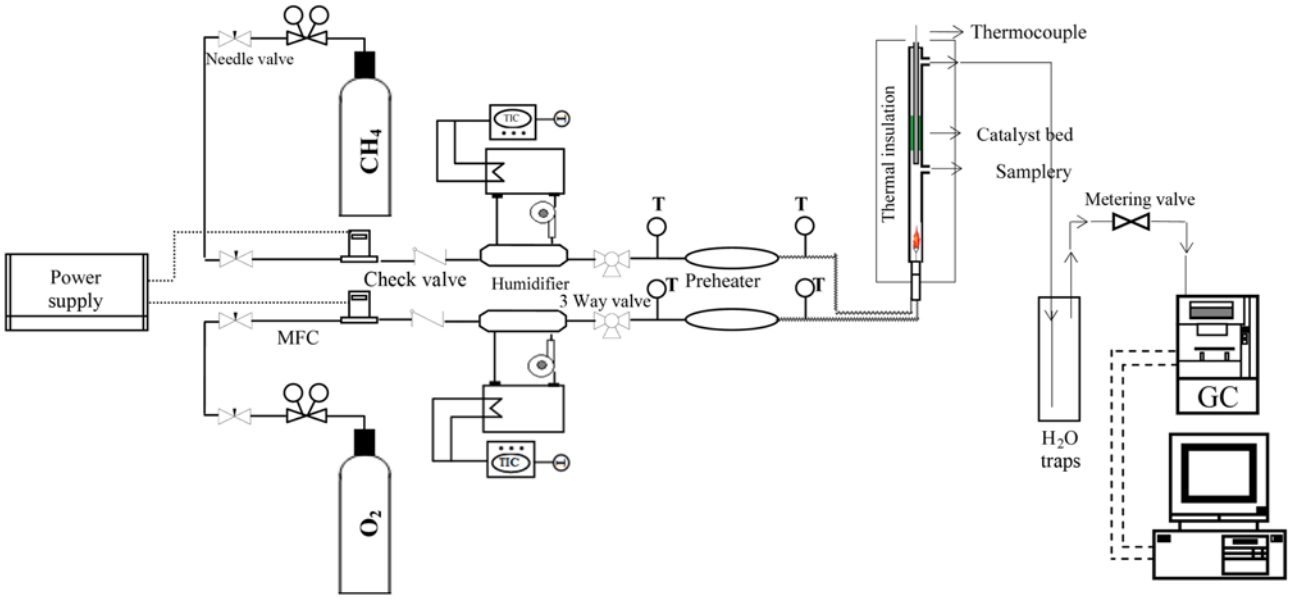

Fig. 1. Schematic diagram of the experimental rig.

combustion chamber and catalyst bed section, was meshed using GAMBIT. The structured hexahedral cells were used to discretize the computational domain, except for the region close to the burner wherein it was necessary to split the reformer domain. This region was meshed into unstructured cells due to complicated burner geometry. To ensure the solution independency from the grid size, the geometry was meshed using four different grid sizes, and the predicted flame temperature in the combustion section as well as H_2 mole fraction at the exit of reactor were used to examine the model grid size independency. Table 1 shows the predicted values for the flame temperature and H_2 mole fraction using the different mesh sizes. The results reveal that the calculated flame temperature for finer control volumes (Grid 2) is approximately 10% smaller than that of Grid 1. The values of calculated flame temperature using the Grids 2 and 3 setups are quite close. However, the difference in the calculated H_2 mole fraction is 3.2% when the Grids 2 and 3 setups were employed. No significant change was observed in the predicted flame temperature and H_2 mole fraction for the Grid 4 setup compared with those predicted for the Grid 3 layout. Therefore, the Grid 3 setup was chosen for the modeling due to the lower required computation time. In this mesh configuration, the whole domain was divided into 338885 tetrahedral cells.

Table 1. Effect of the grid size on the predicted flame temperature and hydrogen mole fraction

	No. of cells	Flame temperature (K)	Mole fraction of H_2 at the exit of reactor
Grid 1	131237	2106	0.3351
Grid 2	272332	1895	0.2976
Grid 3	338885	1888	0.2881
Grid 4	511349	1882	0.2877

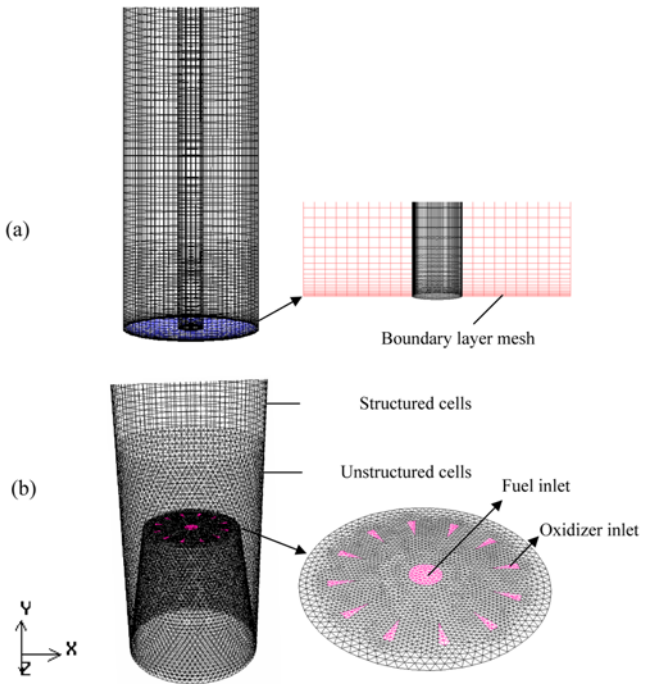

Fig. 2. Mesh configuration in the autothermal reactor: (a) Entrance zone of catalyst bed, (b) Burner and combustion chamber.

Fig. 2 shows an example of meshed configuration of burner, combustion chamber and catalyst bed. As illustrated in the figure, different mesh sizes were used in various places of the modeling domain. The region in the vicinity of the entrance of catalyst bed was meshed into smaller control volumes because of rapid change in reaction rates in this area.

The CFD modeling involves numerical solutions of continuity, momentum, energy and species transport equations. In addition, a user-defined function [28] was written to calculate the reaction rates in the catalyst bed. Gas flow in the reactor was steady, compress-

Table 2. Reaction steps for oxidation of methane and oxygen [2,3]

No	Reaction	A ($cm^3 \cdot mol^{-1} \cdot s^{-1}$)	B	E ($J \cdot mol^{-1}$)
1	$CH_4+H=CH_3+H_2$	2.2×10^4	3	36610
2	$CH_4+OH=CH_3+H_2O$	3.5×10^3	3.08	8368
3	$CH_3+O=CH_2O+H$	6.8×10^{13}	0	0
4	$CH_2O+H=CHO+H_2$	2.2×10^{13}	1.77	13932
5	$CH_2O+OH=CHO+H_2O$	3.4×10^9	1.18	−1870
6	$CHO+H=CO+H_2$	4.0×10^{13}	0	0
7	$CHO+M=CO+H+M$	1.6×10^{14}	0	61505
8	$CHO+O_2=CO+HO_2$	3.3×10^{13}	−0.4	0
9	$CO+OH=CO_2+H$	1.5×10^7	1.3	−3180
10	$H+O_2=OH+O$	5.1×10^{16}	0.82	69078
11	$O+H_2=OH+H$	1.8×10^{10}	1	36945
12	$OH+H_2=H_2O+H$	1.2×10^9	1.3	15188
13	$OH+OH=H_2O+O$	6.0×10^8	1.3	0
14	$H+O_2+M=HO_2+M$	2.1×10^{18}	−1	0
15	$H+OH+M=H_2O+M$	7.5×10^{23}	−2.6	0
16	$HO_2+H=OH+OH$	2.5×10^{14}	0	7950
17	$HO_2+H=H_2+O_2$	2.5×10^{13}	0	2929
18	$OH+HO_2=H_2O+O_2$	5.0×10^{13}	0	4184
19	$O+N_2=N+NO$	1.84×10^{14}	0	320250
20	$N+O_2=NO+O$	6.4×10^9	1	26276
21	$N+OH=NO+H$	3.8×10^{13}	0	0
22	$N_2O+M=N_2+O+M$	1.6×10^{14}	0	215894
23	$N_2O+O=2NO$	1.0×10^{14}	0	117989
24	$N_2O+H=N_2+OH$	7.6×10^{13}	0	63597
25	$CH_3+OH=CH_2+H_2O$	1.5×10^{13}	0	20920
26	$CH_3+H=CH_2+H_2$	9.0×10^{13}	0	63178
27	$CH_2+OH=CH+H_2O$	4.5×10^{13}	0	12552
28	$CH_2+H=CH+H_2$	7.3×10^{17}	−1.56	0
29	$CH_2+OH=CH_2O+H$	3.0×10^{13}	0	0
30	$CH_2+O=CO+H_2$	5.0×10^{13}	0	0
31	$CH_2+O=CO+H+H$	3.0×10^{13}	0	0
32	$CH+H=C+H_2$	1.5×10^{14}	0	0
33	$C+OH=CO+H$	5.0×10^{13}	0	0
34	$CH+O_2=CHO+O$	3.3×10^{13}	0	0
35	$CH+N_2=HCN+N$	1.9×10^{11}	0	56902
36	$HCN+O=NCO+H$	1.4×10^4	2.64	20836
37	$HCN+O=NH+CO$	3.5×10^3	2.64	20836
38	$NCO+H=NH+CO$	5.0×10^{13}	0	0
39	$NH+H=N+H_2$	3.0×10^{13}	0	0

$k=AT^B\exp(-E/RT)$

Table 3. Constants of kinetic rate equations

Kinetic parameters [30]				Adsorption constants [30]			Equilibrium parameters [30]			Kinetic parameters for Ru/Al_2O_3			
Pre exponential factor (kmol/kg h)		Activation energy (kJ/mol)		Species	A (bar^{-1})	ΔH (kJ/mol)	K_i^e	K_{0i}	H_i	Pre exponential factor (kmol/kg h)		Activation energy (kJ/mol)	
$A_1 bar^{-0.5}$	4.225 E+15	E_1	240.1	CH_4	6.65 E-04	−38.28	K_1^e (bar^2)	5.75 E+12	11476	$A_1 bar^{-0.5}$	4.24E+15	E_1	324
$A_2 bar^1$	1.955 E+06	E_2	67.13	H_2O	1.77 E+05	88.68	K_2^e	1.26 E-02	−4639	$A_2 bar^1$	2.1E+06	E_2	59.2
$A_2 bar^{-0.5}$	1.020 E+15	E_3	243.9	H_2	6.12 E-09	−82.90	K_3^e (bar^2)	7.24 E+10	21646	$A_2 bar^{-0.5}$	8.2E+14	E_3	267
				CO	8.23 E-05	−70.65							

ible and turbulent. Mass flow inlet and pressure outlet boundary conditions were set for the burner inlet and the reactor outlet, respectively. Due to the known mixture composition and temperature of reactants at the reactor inlet, the appropriate values were implemented for mass flow rate and temperature of the species. The specific heat of each species was defined as piecewise-polynomial function of temperature. The used under-relaxation factors for pressure, density, momentum, energy and species were 0.12, 0.32, 0.21, 0.94 and 0.91, respectively. In this system, the high rate reactions produce regions with high temperature gradient which cause large change in density. To ensure the stability of solution, small under-relaxation factors were be employed for pressure, density and momentum. In the model, the SIMPLE pressure-velocity coupling algorithm, standard pressure and second order upwind discretization scheme for momentum, energy, turbulent kinetic energy and dissipation energy for all species were employed. For the first convergence criterion, the residuals below 10^{-7} were considered for all variables, while a residual below 10^{-4} was used for the continuity and momentum equations. The second convergence criterion was a condition in which no longer change occurred in averages of temperature and H_2 mass fraction (with iterations) at the exit side. In addition, the mass and energy balances were checked in the whole computational domain in order to find the accuracy of the solved equations.

2. Combustion Reactions Model

The modified standard k-ε model with the $C\varepsilon_1$ value of 1.6 was used to model turbulent behavior in the turbulent region of gas flow [29]. The eddy dissipation concept (EDC) model was used for turbulence-chemistry interaction. A simplified mechanism of methane oxidation, developed by Glarborg et al. [30] and Bilger et al. [31], was employed in the present work. The reactions in the proposed mechanism are listed in Table 2. This mechanism includes 23 species and 39 elementary reactions. Third body efficiencies for all termolecular reactions are 1.0 for H_2, 0.4 for O_2, 6.5 for H_2O, 0.75 for CO, 1.5 for CO_2 and 6.54 for CH_4. The radiation model of discrete ordinates (DO) with WSGGM (weighted sum of gray gas) model was applied to calculate the total emissivity as a function of gas composition and temperature.

3. Catalyst Bed Reactions Model

Due to complications of the reforming process, a simplified reaction mechanism was used in the reforming of methane to give quick estimations on the reformer performance. The proposed global reactions for reforming of methane are [26]:

$$CH_4 + H_2O \Leftrightarrow CO + 3H_2 \qquad \Delta H_1(298\ K) = 206\ kJ/mol \qquad (1)$$

$$CO + H_2O \Leftrightarrow CO_2 + H_2 \qquad \Delta H_2(298\ K) = -41\ kJ/mol \qquad (2)$$

$$CH_4 + 2H_2O \Leftrightarrow CO_2 + 4H_2 \qquad \Delta H_3(298\ K) = 165\ kJ/mol \qquad (3)$$

All reactions are reversible and reactions (1) and (3) represent steam reforming, while reaction (2) is the water gas shift reaction. For these reactions the kinetic rate equations were adopted from Xu and Froment [26] work, which are valid for Ni-based catalyst.

$$r_1 = \frac{k_1}{p_{H_2}^{2.5}}\left(p_{CH_4}p_{H_2O} - \frac{p_{H_2}^3 p_{CO}}{K_1^e}\right)\cdot\frac{1}{den^2} \qquad (4)$$

$$r_2 = \frac{k_2}{p_{H_2}}\left(p_{CO}p_{H_2O} - \frac{p_{H_2}p_{CO_2}}{K_2^e}\right)\cdot\frac{1}{den^2} \qquad (5)$$

$$r_3 = \frac{k_3}{p_{H_2}^{3.5}}\left(p_{CH_4}p_{H_2O}^2 - \frac{p_{H_2}^4 p_{CO_2}}{K_3^e}\right)\cdot\frac{1}{den^2} \qquad (6)$$

Where r_j is presented in $kmol/kg_{cat}s$ and $den=1+K_{CO}\,p_{CO}+K_{H_2}\,p_{H_2}+K_{CH_4}\,p_{CH_4}+K_{H_2O}\,p_{H_2O}/p_{H_2}$. The kinetic rate constants (k_i) are stated in the form of $k_i=A_i.\ \exp(-E_i/RT)$. The first column of Table 3 shows the values of kinetic parameters for each equation (index i:1-3). The second column of Table 3 lists the adsorption constants, K_k, which are represented by $A_k.\exp(-\Delta H_k/RT)$. The index k represents the species including CH_4, H_2O, H_2 and CO. Finally, the equilibrium constants, which are symbolized by $K_i^e=K_{0i}\cdot\exp(-H_i/T)$, are given in the third column of Table 3. The temperature dependence of the rate law parameters for Ru catalyst was obtained from Xu and Froment [26]. Although in our experiments the employed catalyst was not based on Ni, the values related to Ni catalyst were very useful as initial values for validation of CFD results. Consequently, the rate parameters for the three reactions were adjusted until the modeling results matched the experimental data. The values of both A_i and E_i for Ru catalyst are given in the fourth column of Table 3.

RESULTS AND DISCUSSION

Fig. 3(a) shows the experimental results of variation of methane conversion and H_2/CO ratio with temperature. According to this figure, methane conversion increased with increase in inlet fuel (methane and steam) temperature. This can be explained by the fact that the reactor temperature and consequently the thermodynamic methane conversion should be higher at a higher inlet temperature. In addition, as far as reaction rate directly depends on the reactor temperature, a higher temperature can increase the rate of reactions. On the other hand, Fig. 3(a) presents the effect of fuel temperature on the H_2/CO ratio in the product stream. According to these results, increasing of the fuel temperature can significantly increase the H_2/CO ratio. On the other hand, the effects of oxygen to carbon ratio

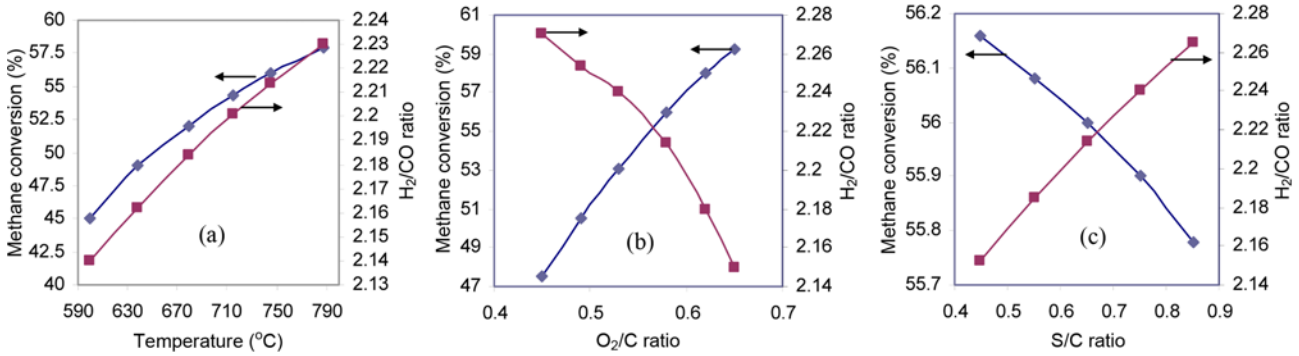

Fig. 3. Effect of (a) fuel temperature (b) oxygen/methane ratio and (c) steam/methane ratio at feed on CH_4 conversion and H_2/CO ratio in products.

on methane conversion and H_2/CO ratio in the product stream are illustrated in Fig. 3(b). As can be seen, with increasing the O_2/C ratio the methane conversion increases and H_2/CO ratio decreases. By increasing of the oxygen molar flow in the feed, the required oxygen for the methane combustion increases and consequently will cause an increase in methane conversion. Moreover, increase in O_2/C ratio causes more heat to be released from the reaction and higher temperature to be established in the reactor. In addition, by increasing the reactor temperature the water gas shift reaction tends to progress in the backward direction and causes an increase in CO and a decrease in H_2 concentration. Therefore, lower H_2/CO ratio was obtained at higher temperature values.

The higher activity of hydrogen with respect to carbon monoxide in reaction with oxygen can be another reason for the observed decrease in H_2/CO ratio in the product stream. From the Fig. 3(c), it can be seen that with the increase of S/C ratio, the conversion of methane decreased and the H_2/CO ratio increased. This can be argued that, in the presence of steam the endothermic reaction of steam reforming occurred and the reactor temperature was decreased and caused a lower rate of methane conversion. On the other hand, with increasing of steam molar flow in the feed and then increase of S/C ratio, the SR and WGS reactions in the catalytic bed tended to forward reaction. Therefore, the produced hydrogen molar flow increased and caused an increase in the H_2/CO ratio. From Fig. 3(b) and 3(c), it can be concluded that the influence of S/C ratio on methane conversion is less than the effect of O_2/C ratio. This can be argued that an increase of O_2/C ratio from 0.45 to 0.65 caused a change of 11.7% in methane conversion. In contrast, the same increase in S/C ratio had not any significant effect on the conversion.

In the first part of modeling, the autothermal reactor was modeled with introducing a fuel temperature of 745 °C, O_2/C ratio of 0.58 and S/C ratio of 0.65. The operating pressure of 1 bar as well as the inlet feed rate of 0.755 mol/h that is equivalent to 4.3584×10^{-6} kg/s were considered. The bed voidage of 0.3 and the thermal conductivity of bed's solid substrate of 1.22 W/mK were considered. In axial and radial directions, the viscous resistance coefficients were set to be 3×10^{9} m^{-2} and 7×10^{10} m^{-2}, respectively. The inertial loss in the catalyst bed was a negligible value because of low velocity. To validate the CFD model, a comparison was done with the measured temperatures and products composition in two parts of reactor. In the first step, the measured temperatures at two points of combustion section (point 1: 2 cm distance from the beginning of reactor; point 2: end of combustion section) were compared with those predicted by CFD. The measured temperatures of the points 1 and 2 were 1,105 k and 1,087 k, while the respective CFD predicted values were 1,090 k and 1,076 k. Therefore, the differences between the measured and predicted values are below 1.36% and a good agreement exists between the model and experimental results. Fig. 4 shows the predicted and measured temperature as a function of dimensionless length (Y_1/L_1) of catalyst bed, in which Y_1 is axial distance from the bottom of catalyst bed and L_1 is the catalyst bed length. The results reveal that the model-predicted temperatures are slightly lower than the measured ones. However, the agreement between experimental and simulated profiles can be acceptable. A sharp decrease in temperature at the beginning of the catalyst bed can be explained by fast rate of endothermic reactions at this region. Fig. 5(a) shows the CFD predicted mole fractions of H_2, CO, CO_2, H_2O and CH_4 as a function of dimensionless length (Y_2/L_2) of combustion section. As before, Y_2 is axial distance from the inlet and L_2 is the combustion section length. The predicted composition profile shows that O_2 was consumed rapidly at the region of Y_2/L_2 less than 0.18, which can be related to very fast mixing at the burner. The results show that the mole fractions of CO_2 and H_2O increase with decrease in O_2 mole fraction and their compositions reach the maximum value. Moreover, the predicted profiles of H_2O and CO_2 reveal decreasing trends, which ultimately reach to fixed values along the axis of reactor. In addition, the H_2 and CO mole fractions increase

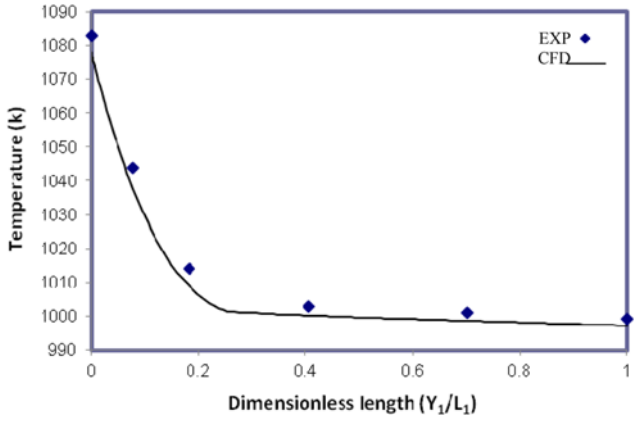

Fig. 4. Experimental and predicted temperatures as a function of dimensionless length of catalyst bed.

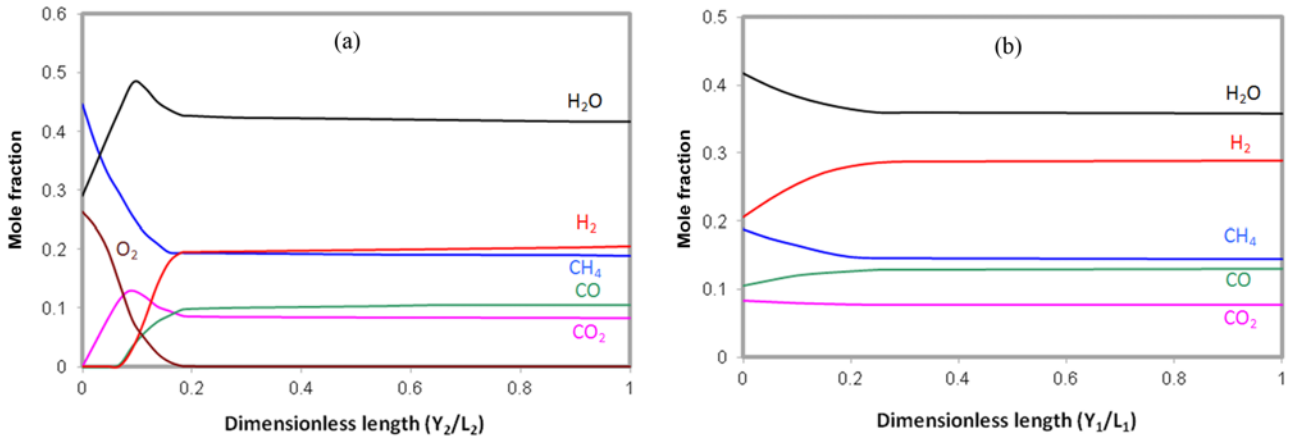

Fig. 5. CFD predicted results of species mole fractions as a function of dimensionless length: (a) Combustion section. (b) Catalyst bed section.

monotonically along the reactor length. The formation of these products begins after formation of H_2O and CO_2. In other words, before production of the H_2O and CO_2, methane was not converted to CO and H_2. The CO and H_2 production reactions were proceeding by decreasing of steam and carbon dioxide concentrations. This figure also demonstrates that CO_2 mole fraction profile reached to its maximum value faster than H_2O, indicating a fast formation of CO_2 at O_2 in consumption step. The product composition and gas temperature at the outlet of combustion section were considered as the feed conditions for the catalytic bed section. The difference percentages between predicted and measured mole fractions in the outlet of combustion section were 4.22% for CH_4, 3.77% for CO_2, 1.92% for H_2O, 5.01% for H_2 and 3.59% for CO. Therefore, it can be concluded that the simulated results are in a good agreement with the experimental data. The CFD predictions of species mole fraction as a function of dimensionless length (Y_1/L_1) of catalyst bed are shown in Fig. 5(b). The profiles show that in the vicinity of the entrance, the average mole fractions of H_2 and CO increase, rapidly. In addition, a sharp decreasing trend in the H_2O and CH_4 mole fractions was obtained. After these rapid changes in profiles, the mole fractions of H_2 and CO increased and those of H_2O and CH_4 decreased slowly along the bed. The results reveal no significant change in CO_2 mole fraction along the catalyst bed. The difference percentages between predicted and measured mole fractions at the outlet of reactor are 7.72% for CH_4, 6.49% for CO_2, 5.40% for H_2O, 7.11% for H_2 and 7.16% for CO.

Fig. 6 shows a comparison between the experimental and modeling methane conversion at different fuel temperatures. It can be seen that there is a good agreement between experimental and modeling results. The results show with increase in temperature, the methane conversion was increased. This can be explained by the fact that in the partial oxidation (POX) section, higher temperature of fuel provides higher molecular energy of reactants that leads to higher

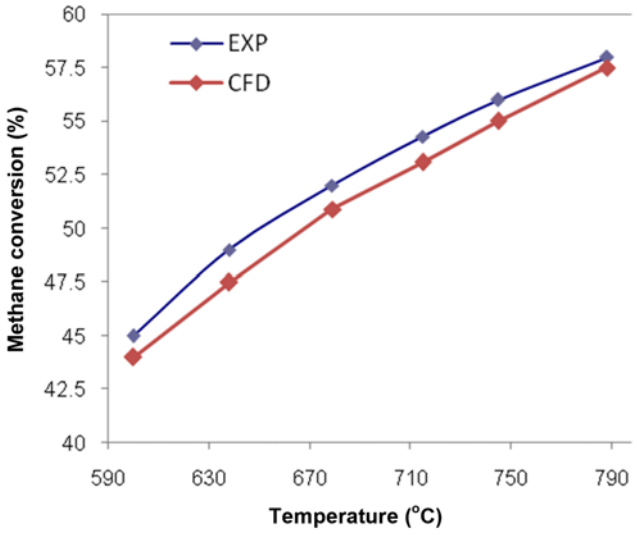

Fig. 6. Comparison between the experimental and predicted methane conversion at different fuel temperatures.

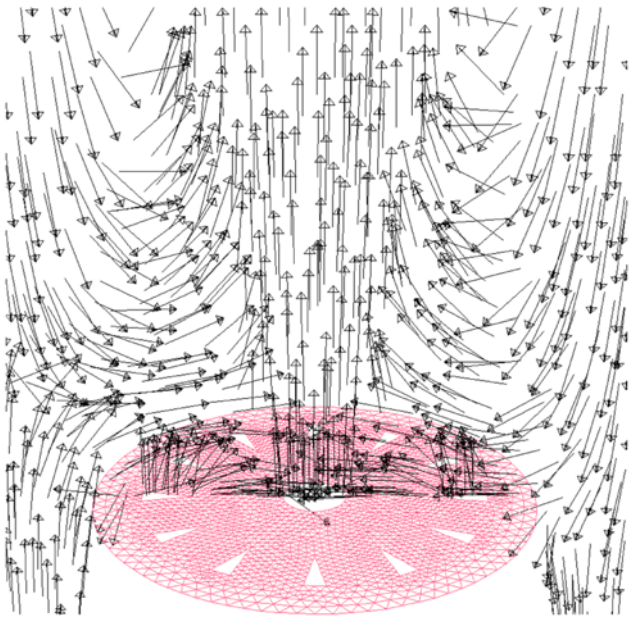

Fig. 7. Velocity vectors plot in a vertical slice in the middle of burner.

rate of methane oxidation. The higher rates of reactions also caused higher released energy in the chamber and higher temperature of products, which are the reactants of steam reforming (SR) section. High temperature of reactants helps the progress of forward reaction in the reversible endothermic SR reaction and leads to higher conversion of methane.

Fig. 7 shows that the velocity vectors in a vertical slice go through the reactor burner. This figure shows that near the burner there is a recirculation zone. The recirculation zone has been generated by the expansion of inlet flow inside the reactor. This recirculation causes a better mixing of hot burnt gases and inlet mixture, which helps to have a stable flame and more efficient reactions. The rapid consumption of O_2 at the region of Y_2/L_2 less than 0.18 (illustrated in Fig. 5(a)) can be explained by this efficient mixing in vicinity of the burner.

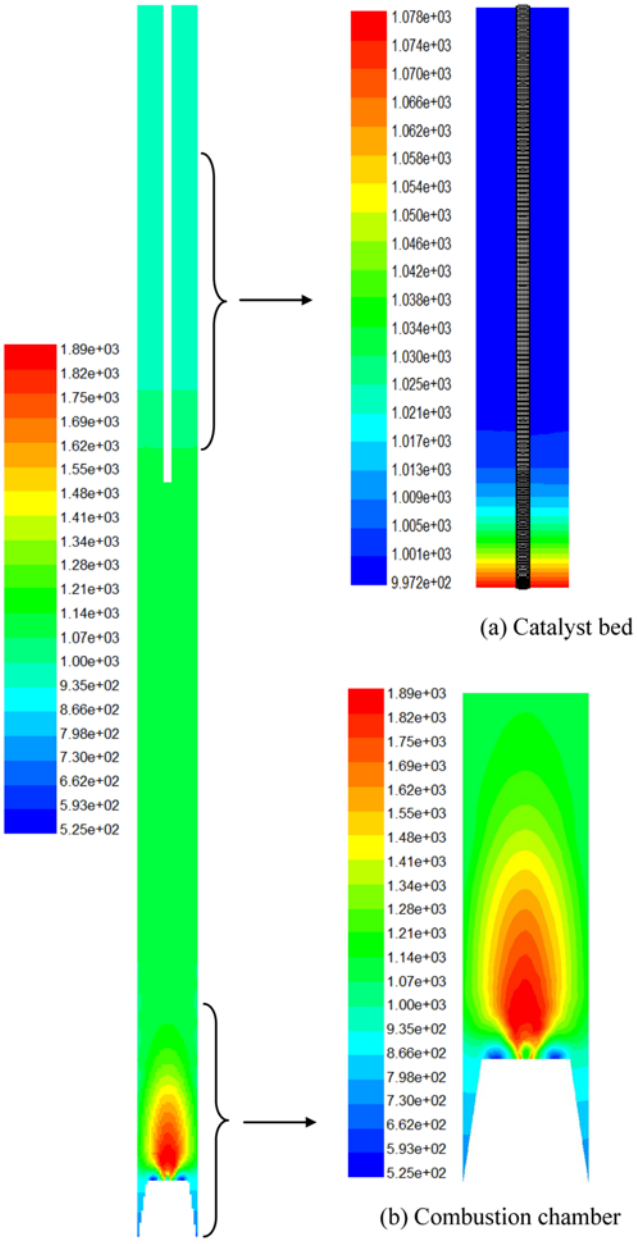

Fig. 8. Contour plot of the temperature (K) distribution in a vertical slice inside the reactor.

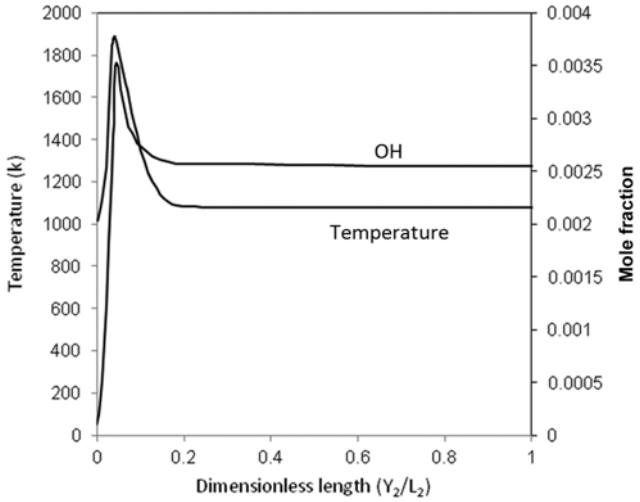

Fig. 9. Variation of temperature and OH mole fraction as a function of dimensionless length of combustion section.

Fig. 8 illustrates the temperature distribution inside the autothermal reactor. As can be seen in the figure, temperature near the burner, where the flame is formed, is higher than other sections inside the reactor. The figure also shows a decreasing trend of temperature in the axial direction in the catalyst bed, where the reforming reaction takes place. In addition, no temperature change can be seen in the radial direction of the catalyst bed.

The OH concentration profile can be used to identify whether combustion occurs inside the reactor [32]. Fig. 9 presents the concentration of OH-radical and temperature profiles along the central axis of the reactor combustion section. As can be seen from the figure, the place of maximum concentration of OH and maximum temperature are both at the flame core. This can be explained by the fact that the OH-radicals emit light when they are changing from their excited state to ground state. Based on a reasonable obtained agreement between the CFD and experimental results, the model predictions and the effects of various thermal conditions on autothermal reforming process have been investigated in the following sections.

1. Effect of Thermal Conductivity of Catalyst Bed on Reactor Efficiency

In this part, the effect of variation of thermal conductivity of porous region on the performance of autothermal reformer was investigated. Four values of thermal conductivity (1.22, 35, 71 and 101 W/mK) were selected. The lower values correspond to catalyst bed with ceramic inert and the higher values are related to catalyst bed with metal inert. The effective thermal conductivity in the porous media is the volume average of the gas and solid conductivities. The temperature distributions in a vertical slice of catalyst bed at four thermal conductivities are shown in Fig. 10(a). The results show that the temperature decreases rapidly in the vicinity of the catalyst bed's entrance, and a bed with lower conductivities causes steeper temperature gradients. This is apparent from the trend of temperature change along the bed, in which the vertical length for temperature change was shortened with decrease in heat conductivity. The predicted temperature differences along the length at Y_1/L_1 less than

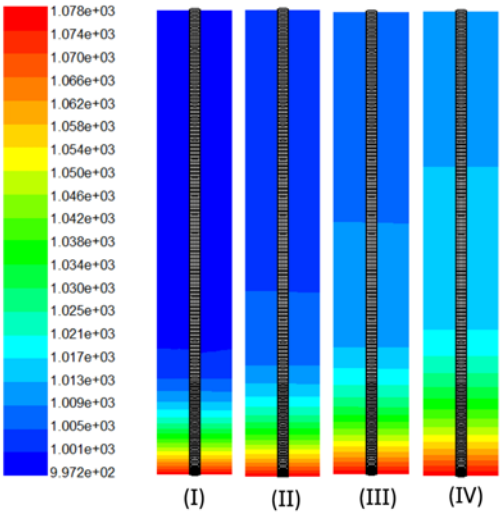

(a) Contour plots of temperature (K) distribution at a vertical slice in the middle of catalyst bed at (I) k =1.22 W/mK, (II) k =35 W/mK, (III) k =71 W/mK, and (IV) k =101 W/m.K.

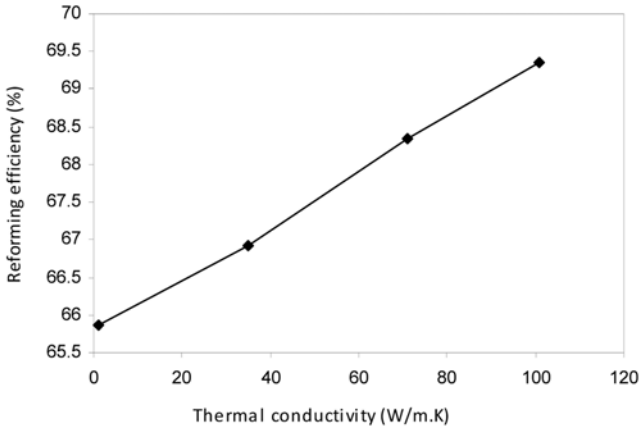

(b) Reforming efficiency based on H_2 at the reactor exit as a function of thermal conductivity

Fig. 10. Effect of thermal conductivity of catalyst bed on (a) Temperature distribution, (b) Reforming efficiency.

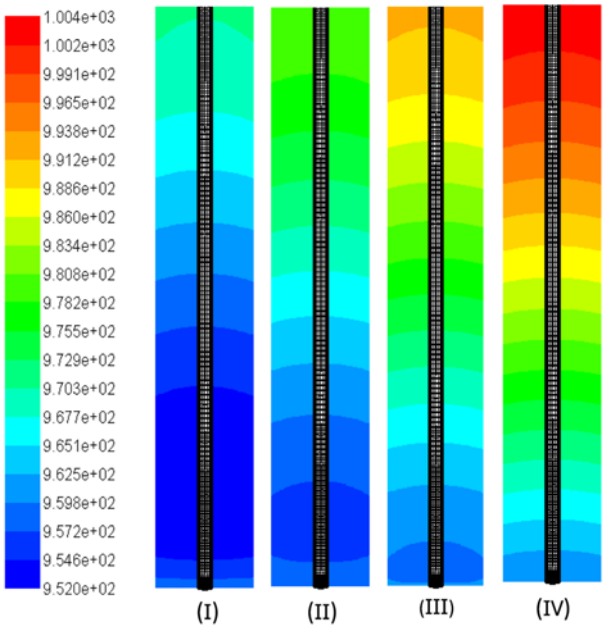

(a) Contour plots of temperature in a vertical slice in the middle of catalyst bed at various heat fluxes (I) 0.5 kw/m^2, (II) 1 kw/m^2, (III) 1.5 kw/m^2, and (IV) 2 kw/m^2

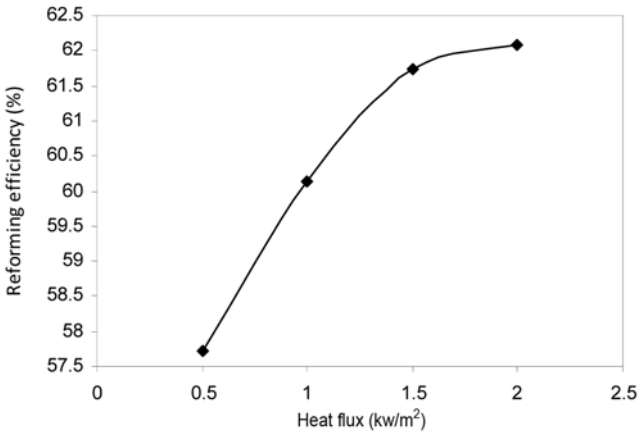

(b) Reforming efficiency based on H_2 at the reactor exit as a function of heat flux

Fig. 11. Effect of wall heat flux on (a) Temperature distribution, (b) Reforming efficiency.

0.2 are 72.31, 65.38, 58.10 and 50.33 K which are related to the thermal conductivities of 1.22, 35, 71 and 101 W/m.K, respectively. This illustrates that as the heat conductivity increased by 82.7 times, the temperature difference of 22 K was obtained at $Y_1/L_1<0.2$.

In the present work, efficiency of reforming process based on H_2 has been defined as follows [17]:

$$\text{Reforming Efficiency} = \frac{\text{LHV of } H_2}{\text{Heat input} + \text{LHV of } CH_4} \quad (7)$$

where LHV is the lower heating value and 'heat input' is the applied heat for the reforming process. The reforming efficiency based on H_2 at the exit of the reactor at various thermal conductivities is presented in Fig. 10(b). This figure shows that with increase in the thermal conductivity of catalyst bed, the reforming efficiency is also increased. It can be argued that due to the increase in heat conductivity and faster heat transfer, the reforming reactions in the catalyst bed are occurring at a higher rate and cause an increase in the reforming efficiency. With increase in thermal conductivity from 1.22 to 101 W/mK, the mole fraction of H_2 at the exit side of reactor is increased from 28.81% to 29.97%, which shows 4.04% increase in H_2 mole fraction.

2. Effect of Heat Flux of Catalyst Bed's Wall on Reactor Efficiency

To investigate the effect of catalyst bed inputted heat flux on the reforming efficiency, a 960 K gas mixture with flow rate and species mole fractions similar to exit gas of combustion section was assumed as an inlet to the catalyst bed. To achieve the same amount of hydrogen mole fraction at the exit side of reactor in an adiabatic condition (0.288), a heat flux of 1 kw/m^2 was inputted to the catalyst bed's wall. In this condition, the predicted maximum temperature

difference across the catalyst bed was approximately 24 K, while with the adiabatic condition this difference was 81 K. Therefore, the temperature difference in adiabatic condition was almost 3.4 times larger than that of constant heat flux. By considering an inlet temperature of 960 K, Fig. 10(a) shows the contour plot of temperature at middle surface of catalyst bed under constant heat fluxes of 0.5, 1, 1.5 and 2 kW/m^2. As shown in this figure, in all setups the outlet temperature of the catalyst bed was more than the inlet temperature. For three cases of 0.5, 1 and 1.5 kw/m^2, the temperature initially decreases at the beginning of the reactor and then grows at the rest of reactor length. This may be due to higher reaction rate at the entrance region because of higher established reactants concentration at this region. As can be seen in Fig. 11(a), with increase in heat flux, the minimum temperature at beginning area is increased and regions with temperature lower than inlet temperature are shortened. Moreover, the lower temperature regions at the beginning of the reactor disappear gradually when the heat flux was increased from 0.5 to 2 kW/m^2. In addition, the modeling results show that the mole fractions of H_2 at the exit side of the reactor are 0.277, 0.288, 0.306 and 0.321 for 0.5, 1, 1.5 and 2 kW/m^2 input heat, respectively. Therefore, a higher heat flux can enhance hydrogen production rate. Fig. 11(b) illustrates the predicted reforming efficiency at reactor exit with various heat fluxes. As can be seen in this figure, the reforming efficiency is increased from 57.73% to 62.07% as the heat flux is increased from 0.5 to 2 kW/m^2. This figure also shows that the increase of heat flux from 0.5 to 1.5 kW/m^2 caused a significant change in the reforming efficiency. However, the results reveal that there is negligible improvement in reforming efficiency by increasing the heat flux from 1.5 to 2 kW/m^2.

CONCLUSIONS

CFD and experimental investigations have been carried out on a noncatalytic autothermal reactor for syngas production. The experimental results showed that with increase in fuel (methane and steam) temperature and O_2/C ratio as well as decrease in ratio of S/C in inlet feed, the methane conversion was increased. On the other hand, it was found that the H_2/CO ratio in product stream increased with increase in fuel temperature and S/C ratio as well as decrease in O_2/C ratio in the reactor feed. The experimental results also revealed that the methane conversion is less sensitive to variation of S/C ratio in inlet feed than change in O_2/C ratio and the fuel temperature. The eddy dissipation concept (EDC) model for turbulence-chemistry interaction in combination with the modified standard k-ε model for turbulence and a chemistry mechanism with 23 species and 39 elementary reactions was considered in the combustion model. A reasonable agreement was achieved between experimental data and the model for species mole fractions and temperature. For the catalyst bed section, the pre-exponential factors and activation energy of kinetic rate constants for the Ru/Al_2O_3 catalyst were obtained by fitting the established model and experimental data. The results revealed that the reforming efficiency and hydrogen mole fraction increase with increase in catalyst bed's thermal conductivity. In addition, the calculated reforming efficiency showed an increase of 4.34% with increase of catalyst bed's heat flux from 0.5 to 2.0 kW/m^2. The model could be used in further studies to find a more accurate value for the optimum heat flux.

NOMENCLATURE

E : total energy [J]
A : pre-exponential factor
E_i : activation energy of reaction i
h : sensible enthalpy [kJ/kg]
h^0 : standard state enthalpy of formation [kJ/kg]
L_1 : length of catalyst bed
Y_1 : axial distance from the bottom of catalyst bed
L_2 : length of combustion section
Y_2 : axial distance from the inlet of combustion section
k : thermal conductivity [w/mk]
k_i : kinetic rate constant of reaction i
P : static pressure [Pa]
M : molecular weight [kg/kgmol]
T : temperature [K]
R_k : net rate of production of species k by reaction [kg/m^3 s]
r_i : reaction rate of reaction i
S/C : molar ratio of steam to carbon in feed
O_2/C : molar ratio of oxygen to carbon in feed
$(-\Delta H)_i$: heat of reaction i
Y_k : local mass fraction of species k

Greek Symbols

μ : molecular viscosity [Pa s]
ρ : density [kg m^{-3}]
γ : porosity of the medium

Subscripts

f : fluid
s : solid
i : reaction index
k : species index
eff : effective

REFERENCES

1. K. Gosiewski, *Chem. Eng. Process*., **39**, 459 (2000).
2. T. S. Christensen and L. L. Primdahl, *Hydrocarbon Process.*, **73**, 39 (1994).
3. K. D. Ko, J. K. Lee, D. Park and S. H. Shin, *Korean J. Chem. Eng.*, **12**, 478 (1995).
4. K. H. Kim, S. Y. Lee, S. W. Nam, T. H. Lim, S. A. Hong and K. J. Yoon, *Korean J. Chem. Eng.*, **23**, 17 (2006).
5. M. S. Lim, M. S. Hong and Y. N. Chun, *Korean J. Chem. Eng.*, **26**, 1022 (2009).
6. K. Koo, J. Yoon, C. Lee and H. Joo, *Korean J. Chem. Eng.*, **25**, 1054 (2008).
7. K. Aasberg-Petersen, T. S. Christensen, C. S. Nielsen and I. Dybkjaer, *Fuel Process. Technol*., **83**, 253 (2003).
8. M. Simeone, L. Salemme, D. Scognamiglio, C. Allouis and G. Volpicelli, *Int. J. Hydrog. Energy*, **33**, 1252 (2008).
9. S. Rabe, T. B. Truong and F. Vogel, *Appl. Catal. A: Gen.*, **292**, 177 (2005).
10. S. C. Dantas, J. C. Escritori, R. R. Soares and C. E. Hori, *Chem. Eng. J.*, **156**, 380 (2010).
11. J. A. C. Dias and J. M. Assaf, *J. Power Sources*, **130**, 106 (2004).

12. S. H. Park, B. H. Chun and S. H. Kim, *Korean J. Chem. Eng.*, **28**, 402 (2011).
13. H. J. Lee, Y. S. Lim, N. C. Park and Y. C. Kim, *Chem. Eng. J.*, **146**, 295 (2009).
14. L. Ma, D. L. Trimm and C. Jiang, *Appl. Catal. A: Gen.*, **138**, 275 (1996).
15. P. M. Biesheuvel and G. J. Kramer, *AIChE J.*, **49**, 1827 (2003).
16. S. H. Chan, D. L. Hoang and O. L. Ding, *Int. J. Heat Mass Transfer*, **48**, 4205 (2005).
17. S. T. Lin, Y. H. Chen, C. C. Yu, Y. C. Liu and C. H. Lee, *J. Power Sources*, **148**, 43 (2005).
18. A. K. Avci, D. L. Trimm and Z. I. Önsan, *Chem. Eng. Sci.*, **56**, 641 (2001).
19. F. Cipitì, L. Pino, A. Vita, M. Laganà and V. Recupero, *Int. J. Hydrog. Energy*, **33**, 3197 (2008).
20. A. Behroozsarand, H. Ebrahimi and A. Zamaniyan, *Ind. Eng. Chem. Res.*, **48**, 7529 (2009).
21. L. Shi, D. J. Bayless and M. E. Prudich, *Int. J. Hydrog. Energy*, **34**, 7666 (2009).
22. X. Zhou, C. Chen and F. Wang, *Chem. Eng. Process.*, **49**, 59 (2010).
23. Y. H. Yu, *Chem. Eng. Technol.*, **25**, 307 (2002).
24. M. Zahedinezhad, S. Rowshanzamir and M. H. Eikani, *Int. J. Hydrog. Energy*, **34**, 1292 (2009).
25. G. A. Karim, A. S. Hanafi and G. Zhou, *J. Energy Res. Technol.*, **115**, 301 (1993).
26. J. Xu and G. Froment, *AIChE J.*, **35**, 88 (1989).
27. H. Amirshaghaghi, A. Zamaniyan, H. Ebrahimi and M. Zarkesh, *Appl. Math. Model.*, **34**, 2312 (2010).
28. Fluent 6.2.16: Fluent Inc., Lebanon (2001).
29. B. B. Dally, D. F. Fletcher and A. R. Masri, *Combust. Theory Model.*, **2**, 193 (1998).
30. P. Glarborg, J. A. Miller and R. J. Kee, *Combust. Flame*, **65**, 177 (1986).
31. R. W. Bilger, S. H. Stamer and R. J. Kee, *Combust. Flame*, **80**, 135 (1990).
32. G. Chen, C. Chen, C. Wu and Y. Chao, *Appl. Catal. A: General*, **332**, 89 (2007).